The Astrophysical Journal, 929:49 (9pp), 2022 April 10 https://doi.org/10.3847/1538-4357/ac59b4

Photon Ring Symmetries in Simulated Linear Polarization Images of Messier 87*

Daniel C. M. Palumbo[1,2] and George N. Wong[3,4]
[1] Center for Astrophysics | Harvard & Smithsonian, 60 Garden Street, Cambridge, MA 02138, USA
[2] Black Hole Initiative at Harvard University, 20 Garden Street, Cambridge, MA 02138, USA
[3] School of Natural Sciences, Institute for Advanced Study, 1 Einstein Drive, Princeton, NJ 08540, USA
[4] Princeton Gravity Initiative, Princeton University, Princeton, NJ 08544, USA
Received 2022 January 31; revised 2022 February 27; accepted 2022 February 28; published 2022 April 12

Abstract

The Event Horizon Telescope (EHT) recently released the first linearly polarized images of the accretion flow around the supermassive black hole Messier 87*, hereafter M87*. The spiraling polarization pattern found in the EHT images favored magnetically arrested disks as the explanation for the EHT image. With next-generation improvements to very long baseline interferometry on the horizon, understanding similar polarized features in the highly lensed structure known as the "photon ring," where photons make multiple half orbits about the black hole before reaching the observer, will be critical to the analysis of future images. Recent work has indicated that this image region may be depolarized relative to more direct emission. We expand this observation by decomposing photon half orbits in the EHT library of simulated images of the M 87* accretion system and find that images of magnetically arrested disk simulations show a relative depolarization of the photon ring attributable to destructive interference of oppositely spiraling electric field vectors; this antisymmetry, which arises purely from strong gravitational lensing, can produce up to ∼50% depolarization in the photon ring region with respect to the direct image. In systems that are not magnetically arrested and with the exception of systems with high spin and ions and electrons of equal temperature, we find that highly lensed indirect subimages are almost completely depolarized, causing a modest depolarization of the photon ring region in the complete image. We predict that next-generation EHT observations of M 87* polarization should jointly constrain the black hole spin and the underlying emission and magnetic field geometry.

Unified Astronomy Thesaurus concepts: Accretion (14); Astrophysical black holes (98); Gravitational lensing (670); Polarimetry (1278); Magnetic fields (994)

1. Introduction

In 2019 April, the Event Horizon Telescope (EHT) released the first image of the accretion flow surrounding the Messier 87 supermassive black hole, hereafter M 87* (Event Horizon Telescope Collaboration et al. 2019a, 2019b, 2019c, 2019d, 2019e, 2019f; hereafter, EHTC I–VI). In 2021 April, the EHT followed up with linearly polarized images (also at the 20 μas angular resolution of the EHT) and identified M 87*'s spiraling polarization structure as the imprint of poloidal magnetic fields threading the accretion flow (Event Horizon Telescope Collaboration et al. 2021a, 2021b; hereafter, EHTC VII–VIII). In this article, motivated by the steadily improving prospects for very long baseline interferometry (VLBI) using longer baselines and higher frequencies, we explore the polarimetric properties of the so-called "photon ring" in simulated images of M 87*. Here, we consider the photon ring to be the image region in which photons arrive at the observer after making one or more half orbits about the black hole.

The properties of polarized light emitted near a black hole have been well studied for decades, especially in the context of X-ray polarization (Connors & Stark 1977; Connors et al. 1980). More recently, efforts to describe the relationship between the local black hole accretion system parameters and the observed submillimeter image have been enabled by improvements in the analytic understanding of the problem. Gralla & Lupsasca (2020a) and Gralla & Lupsasca (2020b) form an excellent primer on the matter of analytic ray tracing in a Kerr spacetime, while Narayan et al. (2021) and Gelles et al. (2021) provide convenient toy models for understanding the physical origin of polarization signatures in the image domain.

In this article, we consider the polarization of direct and indirect lensed images of the accretion flow, for which Johnson et al. (2020) and Himwich & Johnson (2020) make the most relevant predictions. These papers predict symmetry relations between images formed from multiple orbits of photons around the black hole. This paper explores whether these symmetries are present in images produced from general relativistic magnetohydrodynamics (GRMHD) simulations.

Recently, Jiménez-Rosales et al. (2021) observed that in images of GRMHD simulations of M 87*, the photon ring region often has lower fractional polarization than the rest of the more weakly lensed "direct" image. We examine this result by decomposing the image into subimages corresponding to successive photon half orbits and by disentangling two types of depolarization: the destructive interference of oppositely polarized subimages (which decreases total polarization and fractional polarization), and the summation of polarized and unpolarized subimages (which decreases fractional polarization without affecting the total polarization). We focus our analysis on the initial library of GRMHD simulation snapshots produced for EHTC V and considered in Palumbo et al. (2020, hereafter P20).

While the intrinsic depolarization of a particular highly lensed subimage is well explained by Jiménez-Rosales et al. (2021), we explain the destructive interference of polarized

subimages in the context of analytically motivated symmetries of the black hole spacetime using the rotationally symmetric Fourier mode "β_2" described in P20 and used extensively in EHTC VIII. This Fourier mode conveniently describes the appearance of spirals of polarization analogously to E and B modes in studies of the cosmic microwave background (see, e.g., Kamionkowski & Kovetz 2016). The phase of the mode encodes whether the rotationally symmetric pattern of polarization vectors is directed radially, azimuthally, or in between in a handed spiral.

As we will show, the appearance of the accretion flow is highly dependent on the underlying magnetization state, here either standard and normal evolution (SANE) or a magnetically arrested disk (MAD). In MAD flows, significant magnetic flux builds up on the black hole event horizon, increasing the magnetic pressure until it is large enough to counteract the inward ram pressure of the gas and intermittently halt the accretion; by contrast, SANE flows exhibit significantly weaker magnetic fields and thereby have steadier accretion (Ichimaru 1977; Igumenshchev et al. 2003; Narayan et al. 2003). As discussed in P20 and EHTC VIII, MADs are associated with more radial and vertical magnetic fields (collectively, poloidal) in addition to having lower Faraday rotation depths than SANEs.

In this article, we will generally divide results along these magnetization states, black hole spin, and the $R_{\rm high}$ electron heating parameter introduced by Mościbrodzka et al. (2016), which sets the local ratio of electron to ion temperatures according to the ratio of gas and magnetic pressures. Generally $R_{\rm high}$ tunes the dominant emission region and Faraday rotation/optical depths; larger values correspond to greater off-midplane emission and higher rotation/optical depths. For a deeper discussion of the influence of $R_{\rm high}$, see the original text (Mościbrodzka et al. 2016) as well as EHTC V and EHTC VIII.

In keeping with the current literature, we will label lensed accretion flow images by a number n corresponding to the number of photon half orbits between the observer and the termination point of the geodesic. The $n=0$ image thus corresponds to the weakly lensed direct image of the flow, which generally dominates all image metrics including the azimuthal symmetry modes discussed in P20. The $n=1$ image comprises most of the highly lensed emission frequently referred to as the "photon ring" in previous work. Any geodesics with support (that is, with a nonzero flux contribution) in the $n=1$ image will generally also contain flux in the $n=0$ image; the full image can be assembled by summing Stokes parameters over all the subimages.

In Section 2 we provide simple predictions for symmetries of polarization across lensed subimages in flat, Schwarzschild, and Kerr spacetimes with optically thin synchrotron emission. In Section 3 we compute the polarization fraction and azimuthal symmetry metrics for the direct and highly lensed image components in the EHTC V image library. We conclude with a discussion in Section 4.

2. Analytic Predictions

In order to describe spirals of polarization, we use azimuthal Fourier coefficients β_m in the image domain as in P20:

$$\beta_m = \frac{1}{I_{\rm tot}} \int_0^\infty \int_0^{2\pi} P(\rho, \varphi)\, e^{-im\varphi}\, \rho\, {\rm d}\, \varphi\, {\rm d}\, \rho, \quad (1)$$

$$I_{\rm tot} = \int_0^\infty \int_0^{2\pi} I(\rho, \varphi)\, \rho\, {\rm d}\, \varphi\, {\rm d}\, \rho. \quad (2)$$

Here, $P = Q + iU$ is the complex polarization (with Q and U as the usual Stokes parameters), ρ is the image radial coordinate, φ is the image azimuthal coordinate, and $I_{\rm tot}$ is the total Stokes I flux in the image. The β_2 coefficient captures rotationally symmetric polarization structure.

It is instructive to consider the direct image of a particular accretion flow, which we shall embed in different spacetimes. For this purpose, we will use the spiral of the electric vector position angle (EVPA) shown for the time-averaged MAD in Figure 1 (second row, first column). This pattern has $\beta_2 \sim -i$ and thus has phase $\angle\beta_2 \sim -\pi/2$. Recall that for synchrotron emission, which dominates M 87* emission at EHT wavelengths, the polarization is oriented perpendicular to the screen-projected magnetic field in the absence of lensing and Faraday effects.

If viewed from the opposite side, in flat space we would see a spiral of opposite handedness. This flipped view is precisely what a photon sees upon half-orbiting the black hole once in the $n=1$ lensed subimage in a Schwarzschild spacetime. If, however, the EVPA spiral were more akin to the bottom left of Figure 1, with $\beta_2 \sim 1$ (and thus $\angle\beta_2 \sim 0$), we would see that radial EVPA stays radial even when viewed from beneath. Thus when viewing a flow from nearly the top down, as we do for M 87*, the β_2 coefficient for the $n=1$ lensed subimage should appear approximately complex conjugated.

This behavior can be derived analytically in a Schwarzschild black hole spacetime at face-on viewing inclinations through the use of a simple toy model with a few additional simplifying assumptions. Narayan et al. (2021, hereafter N21), predicted the polarization structure produced by a thin, synchrotron-emitting ring of magnetized plasma orbiting a black hole. N21 makes a number of simplifying assumptions about the magnetized fluid: first, that emission is confined to a ring centered on a Schwarzschild black hole, and second, that the fluid velocity and magnetic field are axisymmetric and offset by a constant angle, with equatorial components that are typically assumed to be exactly antialigned (though a vertical magnetic field component is permitted). The ray tracing is simplified as well; N21 traces rays to the equatorial plane analytically using an approximation provided by Beloborodov (2002), which decreases in accuracy with increasing viewing inclination. Optical thinness is also assumed, removing the need for any radiative transfer in favor of a single geometric path-length factor, which does not affect polarization orientation.

In appendix D of N21, they provide approximations for β_2 in terms of the axisymmetric fluid velocity and magnetic field orientation angles χ and η, emission radius R, and equatorial and vertical magnetic field components $B_{\rm eq}$ and B_z. To leading order in the fluid velocity β and lensing factor $1/R$, they find

$$\beta_{2,0} = -\left(1 - \frac{4}{R}\right) e^{2i\eta} B_{\rm eq}^2 + \left(\frac{4}{R} e^{i\eta} - 2\beta e^{i(\eta+\chi)}\right) B_{\rm eq} B_z, \quad (3)$$

where we denote the β_2 coefficient for a particular subimage n by $\beta_{2,n}$.

In order to compute $\beta_{2,n}$ in full generality, we would need to compute the radius of equatorial crossing for all n, which would lose the simplicity of the toy model by violating the assumptions of the underlying Beloborodov approximation made by N21 (Beloborodov 2002). We instead make further

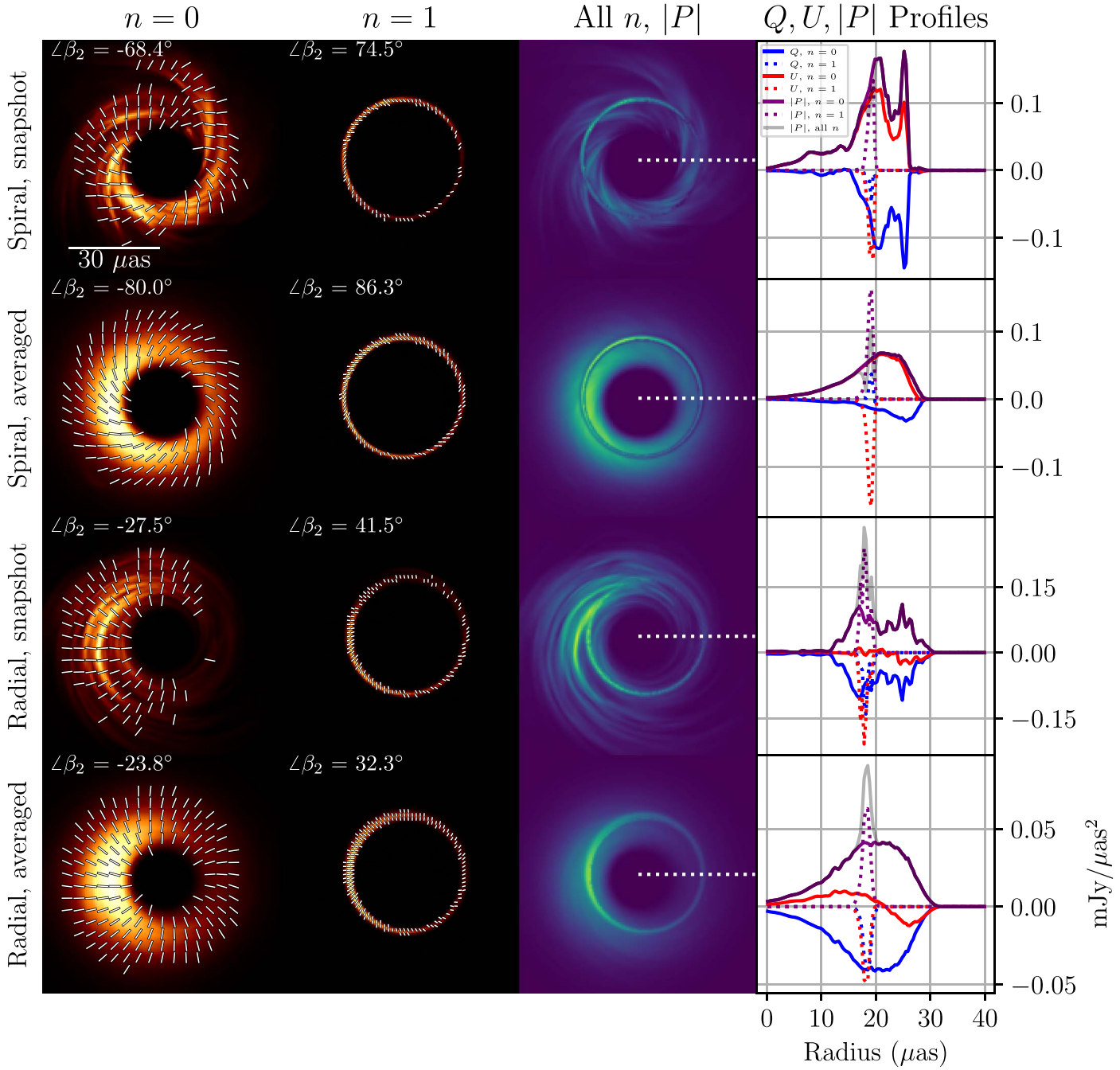

Figure 1. Top row, left column: random snapshot of the $n = 0$ Stokes I subimage from a MAD simulation with $a_* = 0.5$ and $R_{\rm high} = 10$ with EVPA ticks shown where total intensity exceeds 1% of its maximum and fractional polarization is at least 10%. Second column: same as the left column, but $n = 1$. Third column: total linearly polarized flux $|P| = |Q + iU|$ of the full image. Fourth column: profiles of Stokes Q, U, and $|P|$ along the profile depicted as a dotted white line in the third column. Second row: same as the top row, but time-averaged over 200 snapshots across quiescence. Bottom two rows: same as the top rows, but for a SANE simulation with $a_* = 0.94$ and $R_{\rm high} = 1$. Simulations were chosen to have nearly imaginary and nearly real β_2 coefficients, respectively. EVPA spirals change handedness across subimages. For accretion flows with more spiraling magnetic fields and thus less radially directed EVPA, this causes destructive interference near the photon ring, producing the dark depolarized edge in the MAD $|P|$, when direct and indirect images have comparable brightness. In the spiraling model, the subimage partially depolarizes the total image, while in the more radial model, the subimage strictly increases total $|P|$ near the critical curve.

approximations; for photons near the "critical curve" (that is, in Schwarzschild, those photons with screen radius ρ near $\rho_c = \sqrt{27}$ M), the emission radius is essentially constant over n as photons wind nearly circularly about the black hole approaching $R = 3$ M. These circular orbits all impact the equatorial emitting ring at right angles; thus, for all subimages, the emission angle with respect to the Boyer–Lindquist radius is simply $\alpha_G = \pi/2$. This assumption is worst for the $n = 0$ image and essentially eliminates any contribution from vertical fields. Thus, our predictions allow for any axisymmetric magnetic field configuration, although the prediction accuracy decreases as the field becomes more vertical with respect to the midplane.

Finally, we make three additional substitutions to compute the azimuthal symmetry of the nth subimage. For the simple, circular photon orbits of the Schwarzschild spacetime, the

Boyer–Lindquist azimuthal coordinate ϕ swaps sides on each subsequent half orbit. Furthermore, the winding angle ψ must increment by π with each successive half orbit. Finally, the photon angular momentum k with respect to Boyer–Lindquist polar coordinate θ must swap sign each time the photon punctures the midplane in the N21 formalism. Thus, we take

$$\alpha_{G,n} = \frac{\pi}{2}, \tag{4}$$

$$\phi_n = \phi_0 + n\pi, \tag{5}$$

$$\psi_n = \psi_0 + n\pi, \tag{6}$$

$$k_{\theta,n} = (-1)^n k_{\theta,0}. \tag{7}$$

Finally, we compute the full polarization prediction as a function of image azimuthal angle φ and enforce a purely rotationally symmetric polarization by taking a face-on viewer (that is, the viewing inclination $\theta_o \to 0$). We take $\eta = \chi + \pi$ in keeping with the "plasma drags field" assumption taken in N21. We compute the complex polarization P as a function of n and find

$$P_n(\varphi) = \beta_{2,n} e^{i2\varphi}, \tag{8}$$

$$\beta_{2,n} = -e^{i(-1)^n 2\eta} \tag{9}$$

$$= |\beta_{2,0}| e^{i(-1)^n \angle \beta_{2,0}}, \tag{10}$$

$$\to |P_n(\varphi) + P_{n+1}(\varphi)| \propto \text{real}(\beta_{2,0}). \tag{11}$$

In simple terms: for face-on viewing of a flow around a Schwarzschild black hole, the β_2 coefficient asymptotically approaches complex conjugation across subimages for large n and approximately obeys this relation for small $n$for emission near the critical curve, producing a depolarization that depends on the phase of β_2 in image regions with overlapping subimages of adjacent index n. This prediction may be viewed as a zeroth-order approximation for subimage polarization in the N21 model.

In a Kerr black hole spacetime, this conjugation structure does not apply so simply to β_2. This is unsurprising, since a spinning black hole imposes a twisting structure on spacetime that is flipped in handedness across the Boyer–Lindquist midplane. This problem has already been studied in detail by Himwich & Johnson (2020), hereafter H20. In both H20 and N21, conservation of the Walker–Penrose constant κ is used for parallel transport of rays from the observer to the black hole (Walker & Penrose 1970). κ is a property of individual geodesics that encodes the orientation of the polarization vector; for axisymmetric emission from the midplane, κ itself approaches rotational symmetry across geodesics in the observer screen as the observer approaches face-on viewing (as is indicated later by Figure 4). Even along a single geodesic, subsequent midplane crossings yield distinct values of κ since the angle between the magnetic field and the geodesic differs between crossings. In essence, κ is a conserved quantity only for a geodesic that emerges from a single, infinitesimal emitter and otherwise propagates through a vacuum; subimages with distinct n will yield distinct values of κ because the emitting surface is itself distinct, even if the position of arrival on the observer screen is unchanged. This behavior differs from the closely related case of the Carter integral, which is constant along a geodesic regardless of the differing angles between the emission direction and magnetic field at the geodesic origin at each n (Carter 1968).

H20 found that near the critical curve, adjacent subimages exhibit complex conjugation in κ. This behavior is approached at large n; for a single geodesic that encounters the midplane twice (that is, with support in $n = 0$ and $n = 1$), we expect approximate complex conjugation in the value of κ corresponding to the $n = 0$ midplane intersection and the $n = 1$ midplane intersection.

The emission location, observer screen position, and magnetic field geometry specify κ_n, which in turn specifies polarization. The relationship between these parameters and the observed emission is the province of N21 and the extension to Kerr provided by Gelles et al. (2021, hereafter G21) we are more interested in the observable predicted by H20 regarding sums of successive subimages:

$$|P_n(\varphi) + P_{n+1}(\varphi)| \propto \text{real}(\kappa_n) \approx \text{real}(\kappa_{n+1}). \tag{12}$$

Evidently in Kerr, the conjugation symmetry of β_2 is promoted to one of κ, as the axisymmetries of the black hole connect geodesic properties to rotationally symmetric features in the observer screen. In each case, we expect maximum polarization in full (summed over n) images when the direct image value of β_2 or κ is mostly real, and we expect maximum depolarization when the value is mostly imaginary. Note that taking dimensionless black hole spin $a_* \to 0$ and $\theta \to 0$ guarantees $\kappa_{n+1} = \kappa_n^*$ for all rays with support in subimages n and $n+1$, but for more general configurations this statement is approximate, with increasing accuracy at larger n.

Formally, both Equations (11) and (12) are good approximations only for high n in completely optically thin flows. We now summarize the predictions and assumptions for images of simulated flows, which are dominated by low-n emission:

1. We expect complex conjugation between $\beta_{2,0}$ and $\beta_{2,1}$ if emission is viewed nearly face-on. The observer screen radius of the $n = 0$ image is near the critical curve, vertical fields in the emission region are weak, and the black hole has low spin.
2. We expect the same restrictions for complex conjugation between κ_0 and κ_1, but allowing for arbitrary spin.
3. We expect deviations from this behavior in realistic simulations because images at the horizon scale are dominated by low-n structures which only weakly obey symmetries relying on perpendicular impact with an equatorial emission surface.
4. We expect large deviations from both Equations (11) and (12) in models for which there is prominent emission at large radii or far from the equatorial plane.
5. We expect both Equation (11) (if Schwarzschild) and Equation (12) (if Kerr) to hold for arbitrary emission and magnetic field geometries for large n, assuming zero optical depth.

In the next section, we will analyze the GRMHD library largely through the lens of β_2, as β_2 is immediately observationally accessible (given some notion of the image center), while κ is a geodesic property requiring knowledge of the underlying astrophysics. In Section 4, we will touch on whether nearly imaginary κ can produce destructively interfering subimages with nonconjugating β_2 in order to understand trends in the GRMHD simulations.

3. GRMHD Results

We now explore whether the subimage symmetries are present in simulated images of the M 87* accretion flow. We use the GRMHD simulations used for the Stokes I analysis of EHTC V, which were simulated with `iharm3D` (Gammie et al. 2003; Prather et al. 2021) and ray-traced with `ipole` (Mościbrodzka & Gammie 2018). This library consists of five dimensionless black hole spins (-0.94, -0.5, 0, 0.5, and 0.94), two magnetization states (MAD and SANE), and six values of the electron heating parameter $R_{\rm high}$ (1, 10, 20, 40, 80, and 160). The images produced for this paper are for a black hole with mass $= 6.5 \times 10^9\, M_\odot$ at a distance of 16.8 Mpc. These numbers were chosen to match the result of the EHT analysis, although they produce a slightly increased angular size compared to the fiducial image set produced in EHTC V. This change does not noticeably affect any quantities we compute. More details about the simulation pipeline can be found in Wong et al. (2022). The viewing inclination is chosen so that the black hole spin vector is always oriented away from the viewer at an angle of 17° from the screen normal, irrespective of the motion of the accretion disk at large scales. This choice preserves the direction of rotation of the fluid in the inner accretion flow across all models (see Figure 5 in EHTC V and Wong et al. 2021). We have performed the ray tracing anew, using 200 images across the periods of quiescence identified in EHTC V and decomposing emission into $n = 0$ and $n = 1$ subimages at a resolution of $1/3$ μas. This decomposition follows the scheme in Johnson et al. (2020), in which subimages are delineated by turning points in Boyer–Lindquist θ along photon geodesics.

In Figure 1, we examine a MAD with $a_* = 0.5$ and $R_{\rm high} = 10$ and a SANE with $a_* = 0.94$ and $R_{\rm high} = 1$. We choose these two models because they lead to spiraling and radial EVPA patterns, respectively. The profiles in the right column of the figure show patterns in polarized flux with a few notable features consistent with our analytic intuition: first, the spiraling model appears depolarized in some regions near the photon ring, while the radial model has a strictly increased polarized flux profile. In the spiraling model, where the peak brightness of the photon ring exceeds the direct image brightness, we see a pair of dark bands surrounding a brighter ring of polarization. These dark bands correspond to the points in the $n = 1$ profile where $P_{n=1}$ is equal and opposite to $P_{n=0}$; where $P_{n=1}$ is at its maximum, the total polarization can exceed the $n = 0$ profile even if the overall structure exhibits depolarization, as seen in the second row, fourth column of Figure 1. Ultimately, the flux ratio between the $n = 0$ and $n = 1$ image determines whether a single dark photon ring region or two dim bands are present in $|P|$. Note that two types of depolarization can be present in general: one in which an unpolarized and polarized image are summed, decreasing fractional polarization m but not total polarized flux $|P|$, and another in which polarization interferes destructively, decreasing both m and $|P|$. The dark bands in $|P|$ are clear evidence of the latter type.

We now turn to analyzing the full set of $n = 0$ and $n = 1$ images for the GRMHD image library introduced earlier. We compute the β_2 coefficient with one major difference from P20—we do not blur the image by the nominal 20 μas resolution of the 2017 M 87* EHT data. We are not interested in the bulk properties of the flow that can be inferred from a blurry image. Rather, we aim to identify whether or not subimages exhibit near-conjugation symmetries in the β_2 coefficient, and the blurring procedure is orthogonal to this consideration. In any case, blurring generally depolarizes the image and suppresses high-frequency modes in the azimuthal Fourier decomposition; the effect of a 20 μas blur on β_2 is to slightly reduce amplitude while leaving the phase essentially unchanged.

Figure 2 shows the complex β_2 coefficients for each set of simulation and image parameters for both $n = 0$ and $n = 1$. Recalling from EHTC VIII that the β_2 amplitude is essentially redundant with the average linear polarization fraction in an image, we note that any set of images with nearly zero $|\beta_2|$ is also nearly completely depolarized. Thus, we observe several general trends:

1. Increasing $R_{\rm high}$ weakly depolarizes the $n = 0$ image and greatly depolarizes the $n = 1$ image, particularly in MADs.
2. Images with significant fractional polarization in the $n = 1$ component exhibit nearly conjugated β_2 coefficients between $n = 0$ and $n = 1$, with the largest deviation from this behavior occurring for retrograde MADs, particularly those with $a_* = -0.94$.
3. In all cases except the $R_{\rm high} = 1$ prograde spinning SANEs, SANE $n = 1$ images are almost completely depolarized.

These results follow trends identified in EHTC VIII: higher $R_{\rm high}$ depolarizes images overall and SANEs are typically more innately magnetically scrambled and are less polarized. Moreover, higher values of $R_{\rm high}$ correspond to stronger emission from the jet as opposed to the accretion flow. Emission from farther out from the equatorial plane disobeys the assumptions required for the H21 symmetries, which may also contribute to violations of the equatorial emission predictions (though Faraday effects likely dominate).

The retrograde high-spin MAD results are peculiar in that $\beta_{2,0}$ and $\beta_{2,1}$ are almost exactly opposite, reflecting an overall sign flip rather than a complex conjugation. Recall, however, that for general viewing angles, spins, magnetic fields, and emission geometries, we only expect approximate complex conjugation of the underlying κ, not β_2. Although κ cannot be extracted simply from a polarized image, we will discuss later an example fluid configuration that can give rise to the MAD $a_* = -0.94$ pattern.

Next, we examine depolarization near the critical curve. Rather than set a mask based on possible photon ring locations as in Jiménez-Rosales et al. (2021), we simply generate a mask using our ray-traced $n = 1$ images. Within the $n = 1$ image, wherever the Stokes I flux exceeds 1% of its peak value, we consider the pixel to be in the "photon ring region." We use this mask on the full, all-n image to select photon ring pixels and compute the Stokes I–weighted fractional polarization as in EHTC VII. The details of these masking choices are not particularly relevant to the signal we are seeking: qualitatively, the full image should depolarize according to Equation (11) for face-on, Faraday/optically thin emission. As we have seen in Figure 2, these assumptions are violated for almost all SANEs, as the indirect emission is almost completely depolarized. Thus, our expectation is that the average Stokes I–weighted fractional polarization near the critical curve in MADs should obey $\langle |m_{\rm avg}| \rangle_I \propto 1 - \sin|\angle \beta_2|$, since more spiraling EVPA patterns cancel with their subimage. In SANEs, where the $n = 1$ image is generally depolarized, the polarized $n = 0$

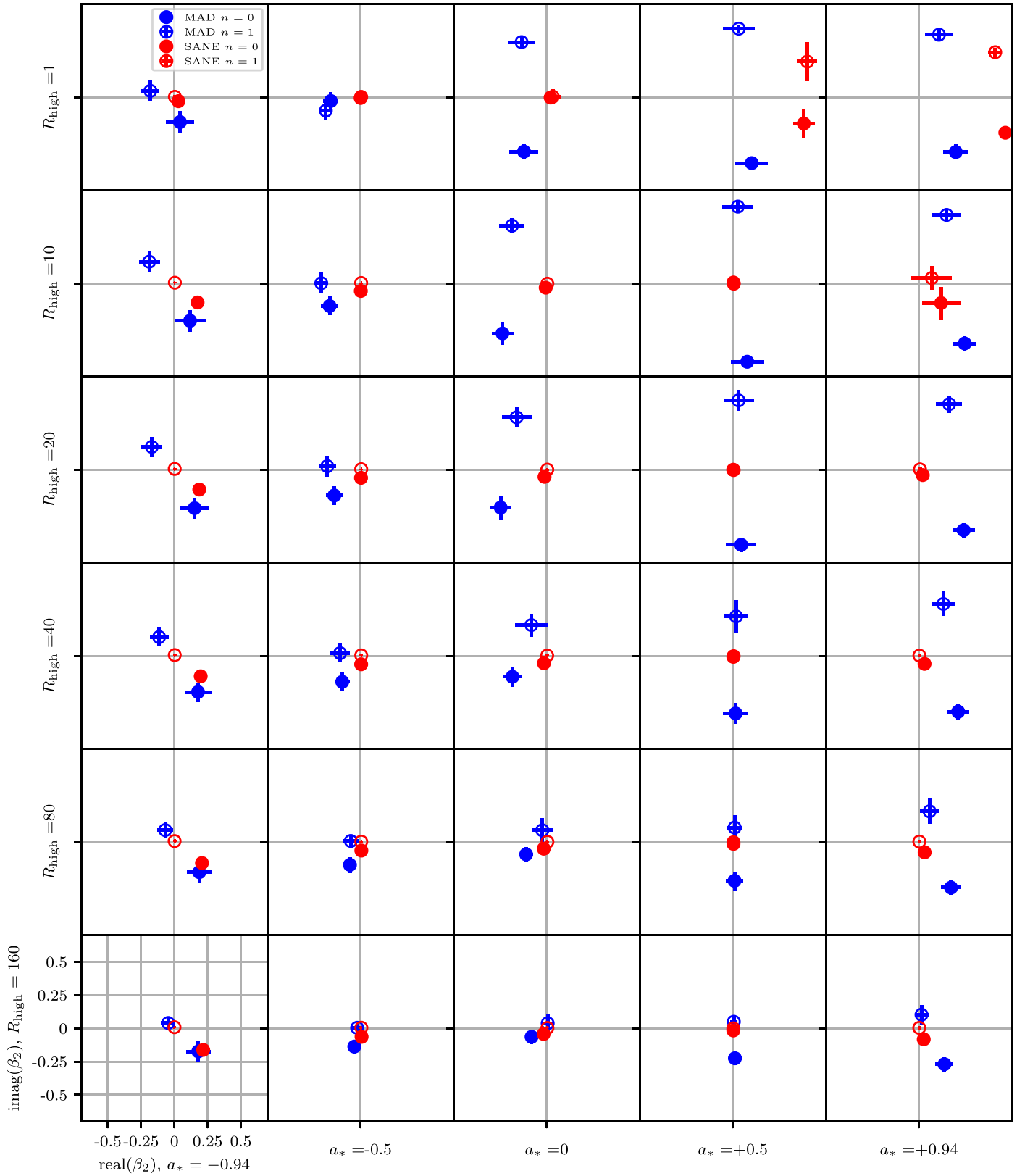

Figure 2. Values of the complex rotational symmetry coefficient β_2 for $n = 0$ and $n = 1$ subimages across MAD and SANE simulations of varying spin and $R_{\rm high}$. Scale is constant across the grid; nonaxial grid lines are hidden for clarity.

image is added to an unpolarized $n = 1$ image, causing a net decrease in average fractional polarization. This decrease does not depend on $\angle\beta_2$, because the $n = 1$ image is not polarized.

Figure 3 shows the full-image-to-subimage ratio of the Stokes I–weighted fractional polarization $\langle|m|\rangle_I$ for MADs and SANEs at $R_{\rm high} = 10$ and 80 (corresponding to the second and fifth rows of Figure 2). If the mechanism for depolarization is

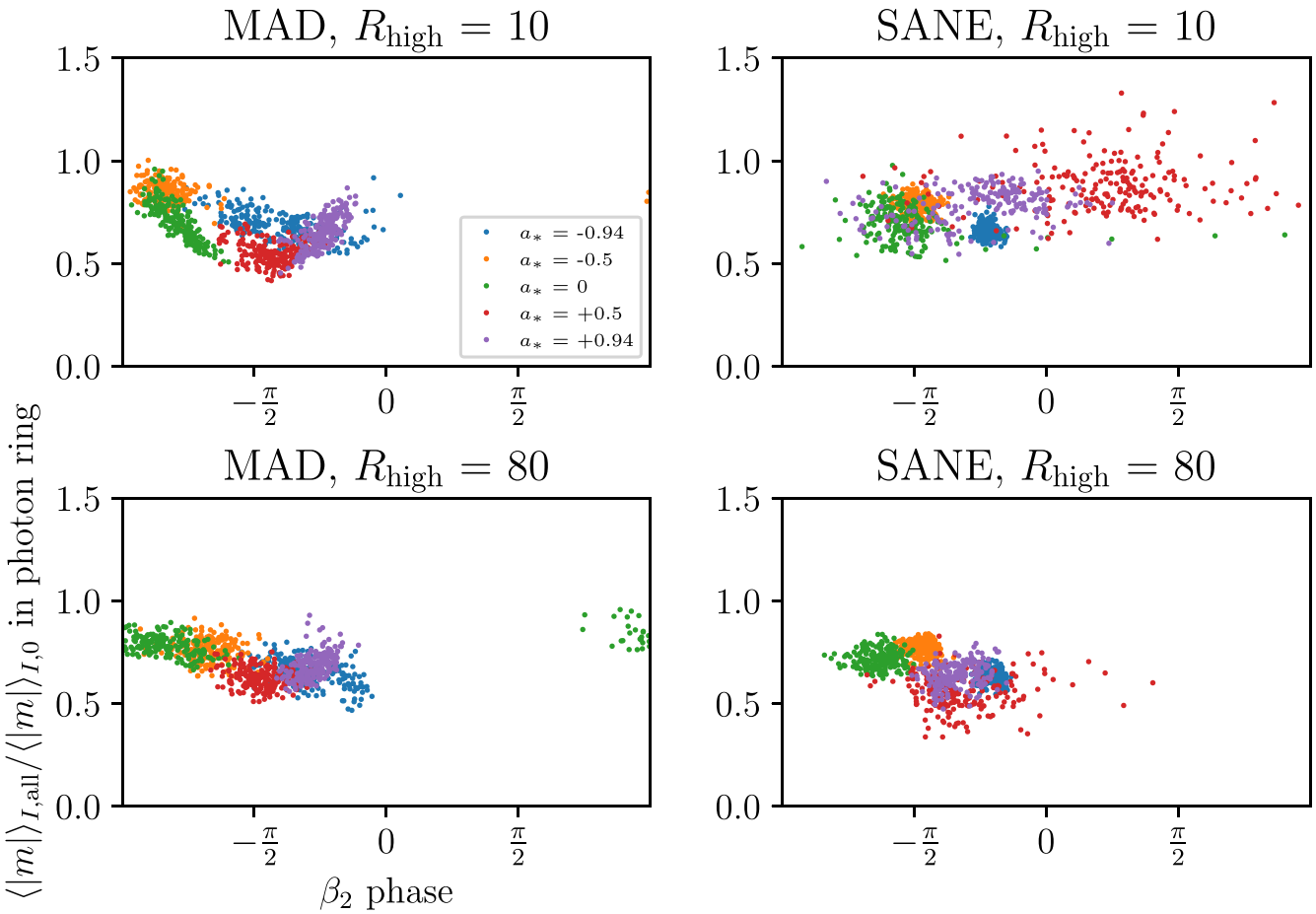

Figure 3. Top left: ratio of average fractional polarization in the all-n image to that in the $n = 0$ image plotted against the phase of the rotationally symmetric β_2 coefficient for images from a MAD model with $R_{\rm high} = 10$. Right: same as the left, but for SANE images. Bottom row: same as the top row, but for $R_{\rm high} = 80$. Images of prograde MADs exhibit sinusoidal behavior with respect to $\angle\beta_2$ due to destructive interference of oppositely handed EVPA spirals, while SANEs appear depressed by a roughly constant factor.

indeed the destructive interference between oppositely handed spirals, the depolarization between the $n = 0$ and all-n images should be largest at $\angle\beta_2 = -\pi/2$; this is very visible as a "U" shape in the top left panel of the figure. At high $R_{\rm high}$ values, however, the subimage is significantly depolarized, and adding a depolarized background to a polarized foreground weakens the dependence on $\angle\beta_2$, as can be seen in the bottom left. When the subimage is most polarized and oppositely spiraling, as in the $R_{\rm high} = 10$ MADs with $a_* = 0.5$, this destructive interference reduces the fractional polarization in the photon ring region by 50% (a result that is sensitive to our choice of photon ring mask criterion). Meanwhile, the SANEs fall roughly in a horizontal line regardless of $R_{\rm high}$, indicating that the spiral interference is a negligible contribution to the depolarization.

As an aside, most images—including nearly all MADs—are confined to negative values of the β_2 phase, corresponding to a strict adherence to the assumption made in N21, i.e., that the magnetic field trails the fluid velocity. For a clockwise flow on the sky (here, dictated by our choice of viewing inclination), this assumption requires $-\pi < \angle\beta_2 < 0$. Prograde $a_* = 0.5$ SANEs with $R_{\rm high} = 10$, however, are so close to the origin in the complex β_2 plane that the phase of β_2 wanders significantly even at quiescence.

We conclude then that the dominant depolarization mechanism in the photon ring regions of MADs (especially at low $R_{\rm high}$) is the cancellation of EVPA spirals across subimages, whereas for SANEs and MADs at very high $R_{\rm high}$ the mechanism is more likely the addition of an unpolarized $n = 1$ image. Note that this effect is distinct from the depolarization of any individual subimage, for which optical depth and Faraday effects governed by magnetic fields, electron temperature, and density will be dominant; see Jiménez-Rosales et al. (2021) for a discussion of intrinsic depolarization of the long geodesics in the photon ring.

4. Discussion

We have computed the rotational symmetry coefficient β_2 for $n = 0$ and $n = 1$ subimages from a large library of GRMHD simulations and found clear evidence for complex conjugation of the coefficient in almost all MADs and almost no SANEs. We found that the relative depolarization of the photon ring with respect to other image regions is greatest in MADs with $|\angle\beta_2| \sim \pi/2$. The almost universal depolarization of the $n = 1$ image in SANE simulations suggests that any depolarization of the photon ring region comes from the sum of polarized and unpolarized subimages rather than destructive interference. Collectively, we reproduce the result in Jiménez-Rosales et al. (2021) that the photon ring is often depolarized relative to the rest of the image and find a compelling case that, at low values of $R_{\rm high}$, this relative depolarization is primarily due to lensing symmetries. We attribute deviation from the complex

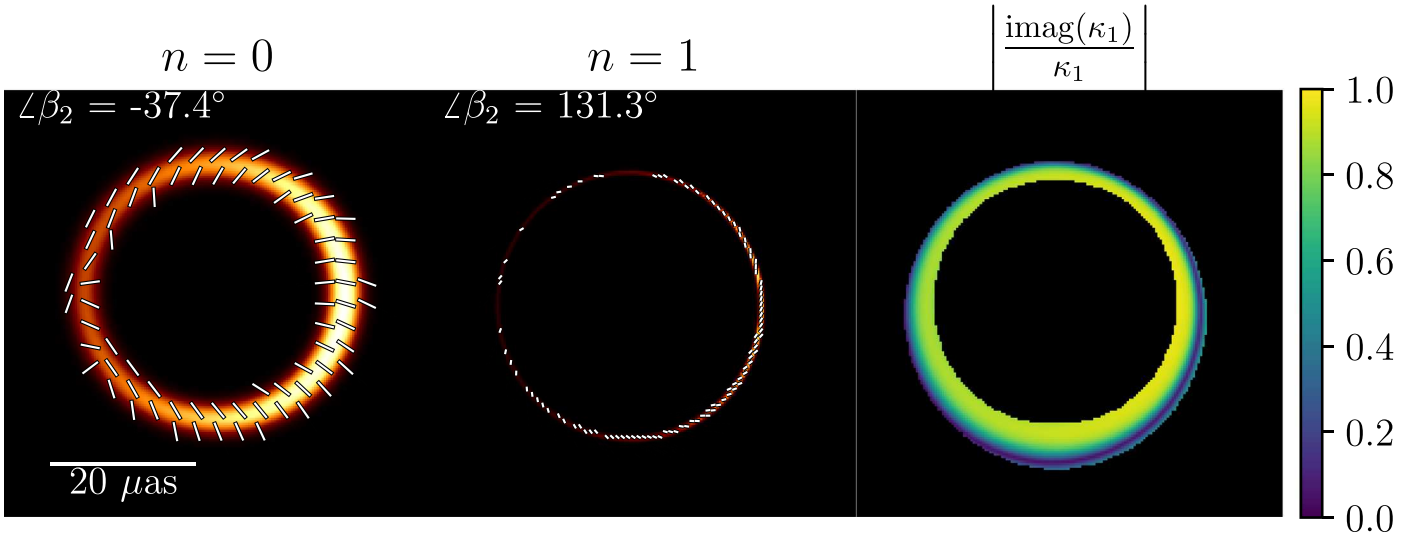

Figure 4. Example Gelles et al. (2021) toy model for a synchrotron-emitting ring of polarized gas chosen to produce the β_2 phase offset seen in MADs with $a_* = -0.94$ in Figure 2. Left two columns: predicted $n = 0$ and $n = 1$ images shown with same plotting parameters as Figure 1. Right column: fractional imaginary part of the Penrose–Walker constant κ underlying the predicted images (brighter corresponds to more imaginary). The nearly 180° rotation in $\angle\beta_2$ corresponds to a nearly 90° uniform rotation in EVPA between $n = 0$ and $n = 1$ as predicted by Himwich & Johnson (2020) for (nearly) purely imaginary κ.

conjugation of β_2 to prominent effects from spin, optical and Faraday rotation depth, and emission originating at large radii or far from the equatorial plane of the black hole.

We have found that retrograde highly spinning MADs (of any $R_{\rm high}$) do not exhibit obvious complex conjugation of β_2 (see the left column of Figure 2). As is apparent in Figures 2 and 3, these models are still heavily depolarized by the destructive interference of the $n = 1$ image, but here $\beta_{2,1}$ is nearly the negation of the direct image value. We investigate this behavior by reproducing it using the G21 toy model evaluated over an observer screen; we use the Kerr Bayesian accretion modeling (`KerrBAM`) code (Palumbo et al. 2022, in preparation) to generate images. We find that a broad class of models can reproduce the MAD $a_* = -0.94$ behavior when supplied with reasonable model parameters for such a flow. Nonzero inclinations, strong vertical fields, and emission at radii far from $R \approx \sqrt{27} - 1$ M can all create large deviations from the conjugation symmetry. As one example, Figure 4 considers a model of an emissive ring viewed at $\theta_o = 17°$ with a Gaussian profile centered at 3 M with a full width at half maximum of 1 M and a predominantly radially infalling gas moving at $\beta = 0.6$ with a nonnegligible vertical field ($\chi = -7\pi/8$, $\eta = \chi + \pi$, and $B_z = 0.5$ in the terminology of N21). Here, distances are expressed in scale-free units, where $1\,\mathrm{M} = GM/c^2$ for the gravitational constant G, black hole mass M, and speed of light c. We find a nearly 90° offset in EVPA ($\sim$180° in $\angle\beta_2$) between the $n = 0$ and $n = 1$ subimages, corresponding to the half-rotation in the complex plane seen in the $a_* = -0.94$ MADs. As expected, the underlying κ is almost purely imaginary, with the exception of a narrow band far from the critical curve, giving rise to destructive interference through Equation (12).

This replication is notable because the toy model is purely equatorial; we expect that in addition to the emission radius and magnetic field caveats, three-dimensional emission geometries (as seen in Figure 4 of EHTC V) would also cause a breakdown of the simple subimage relations. Chael et al. (2021) found that in time-averaged simulations of MAD accretion flows, emission is concentrated in a relatively thin region about the equatorial plane, which may mitigate violations of these simple symmetries. However, as we see in Figure 4, complicated three-dimensional geometry is not required to produce relations between subimage polarization patterns that violate simple flat space intuition. It is thus remarkable that so many of the GRMHD models obey the simpler Equation (11) relation despite the complicated structure of the spacetime geometry and emission features; we attribute this to the conclusion in EHTC V that the majority of emission in the GRMHD library tends to come from radii near 4.5 M. As is evident from the "just add one" approximation that the lensed screen radius of emission from a radius R appears nearly at $\rho \approx R + 1$ for face-on viewing geometries, emission from near $R = 4.5$ M will fall near the critical curve, which is the most impactful requirement for applying Equations (11) and (12). Moreover, we expected strong vertical fields to create large discrepancies from Equation (11); however, as touched on in Event Horizon Telescope Collaboration et al. (2021b) and Narayan et al. (2021), vertical magnetic fields near the equatorial plane in GRMHD (and likely in M 87*) tend to be fairly weak.

In this article, we have only considered linear polarization. Recently, Moscibrodzka et al. (2021) and Ricarte et al. (2021) found that the photon ring region in images of GRMHD simulations often has the opposite sign of circular polarization compared to the direct image of the flow. Although this signature appears similar to the lensing symmetries discussed here, the circular polarization antisymmetry is due to subtle details of the underlying magnetic field and its twist, and is a less generic property of roughly disk-like flows about a black hole. Moreover, since the N21/G21 toy model we consider in this paper does not consider polarized radiative transfer, it is insufficient for a detailed study of circular polarization, so more work remains in generating as intuitive a picture for circular polarization as has been done for linear polarization.

Given the conclusion of EHTC VIII that M 87* is likely magnetically arrested, we expect that future high-resolution VLBI measurements of the M 87* photon ring should find slight depolarization near the critical curve due to M 87*'s gently spiraling EVPA pattern and low overall polarization. Further, the so far consistent story that M 87*'s compact 230 GHz emission is

from somewhere in the 3–5 M range of radii with weak vertical fields favors the application of the symmetries identified here and in Himwich & Johnson (2020). This is of particular relevance to the next generation Event Horizon Telescope (ngEHT; see, for example, Raymond et al. 2021), for which a primary objective is polarized studies of the M 87* $n = 1$ subimage. The variety of β_2 phase offset structures in Figure 2 suggests that a measurement of the $n = 0$ and $n = 1$ polarization spirals would simultaneously constrain multiple properties of the black hole accretion system. While the black hole spin is constrained through the shape of the photon ring itself, the astrophysical details are inextricably linked to the spacetime through κ and encoded in the relation between $n = 0$ and $n = 1$ polarization, meaning that model-fitting the magnetic field and plasma around the black hole might pin down the fluid velocity, magnetic field geometry, and the location of the emission in addition to parameters of the spacetime. We remain hopeful that within the decade, we will have a formal, if imprecise, constraint on the three-dimensional emission and magnetic field geometry of M 87*.

We thank Elizabeth Himwich, Ramesh Narayan, Monika Mościbrodzka, Zachary Gelles, Angelo Ricarte, and Michael Johnson for many helpful early discussions, as well as Thomas Bronzwaer for a thorough review of early drafts. We also thank our reviewer for their thoughtful comments on our manuscript. This work was supported by the Black Hole Initiative at Harvard University, which is funded by grants from the John Templeton Foundation and the Gordon and Betty Moore Foundation to Harvard University. D.C.M.P. was supported by National Science Foundation grant Nos. AST 19-35980 and AST 20-34306. G.N.W. gratefully acknowledges support from the Institute for Advanced Study.

Software: `eht-imaging` (Chael et al. 2018), `ipole` (Mościbrodzka & Gammie 2018), `KerrBAM` (Palumbo et al. 2022, in preparation), Matplotlib (Hunter 2007), Numpy (Harris et al. 2020).

ORCID iDs

Daniel C. M. Palumbo https://orcid.org/0000-0002-7179-3816
George N. Wong https://orcid.org/0000-0001-6952-2147

References

Beloborodov, A. M. 2002, ApJL, 566, L85
Carter, B. 1968, PhRv, 174, 1559
Chael, A. A., Johnson, M. D., Bouman, K. L., et al. 2018, ApJ, 857, 23
Chael, A., Johnson, M. D., & Lupsasca, A. 2021, ApJ, 918, 6
Connors, P. A., Piran, T., & Stark, R. F. 1980, ApJ, 235, 224
Connors, P. A., & Stark, R. F. 1977, Natur, 269, 128
Event Horizon Telescope Collaboration, Akiyama, K., Alberdi, A., et al. 2019a, ApJL, 875, L1
Event Horizon Telescope Collaboration, Akiyama, K., Alberdi, A., et al. 2019b, ApJL, 875, L2
Event Horizon Telescope Collaboration, Akiyama, K., Alberdi, A., et al. 2019c, ApJL, 875, L3
Event Horizon Telescope Collaboration, Akiyama, K., Alberdi, A., et al. 2019d, ApJL, 875, L4
Event Horizon Telescope Collaboration, Akiyama, K., Alberdi, A., et al. 2019e, ApJL, 875, L5
Event Horizon Telescope Collaboration, Akiyama, K., Alberdi, A., et al. 2019f, ApJL, 875, L6
Event Horizon Telescope Collaboration, Akiyama, K., Algaba, J. C., et al. 2021a, ApJL, 910, L12
Event Horizon Telescope Collaboration, Akiyama, K., Algaba, J. C., et al. 2021b, ApJL, 910, L13
Gammie, C. F., McKinney, J. C., & Tóth, G. 2003, ApJ, 589, 444
Gelles, Z., Himwich, E., Johnson, M. D., & Palumbo, D. C. M. 2021, PhRvD, 104, 044060
Gralla, S. E., & Lupsasca, A. 2020a, PhRvD, 101, 044032
Gralla, S. E., & Lupsasca, A. 2020b, PhRvD, 101, 044031
Harris, C. R., Millman, K. J., van der Walt, S. J., et al. 2020, Natur, 585, 357
Himwich, E., Johnson, M. D., Lupsasca, A. r., & Strominger, A. 2020, PhRvD, 101, 084020
Hunter, J. D. 2007, CSE, 9, 90
Ichimaru, S. 1977, ApJ, 214, 840
Igumenshchev, I. V., Narayan, R., & Abramowicz, M. A. 2003, ApJ, 592, 1042
Jiménez-Rosales, A., Dexter, J., Ressler, S. M., et al. 2021, MNRAS, 503, 4563
Johnson, M. D., Lupsasca, A., Strominger, A., et al. 2020, SciA, 6, eaaz1310
Kamionkowski, M., & Kovetz, E. D. 2016, ARA&A, 54, 227
Mościbrodzka, M., Falcke, H., & Shiokawa, H. 2016, A&A, 586, A38
Mościbrodzka, M., & Gammie, C. F. 2018, MNRAS, 475, 43
Moscibrodzka, M., Janiuk, A., & De Laurentis, M. 2021, MNRAS, 508, 4282
Narayan, R., Igumenshchev, I. V., & Abramowicz, M. A. 2003, PASJ, 55, L69
Narayan, R., Palumbo, D. C. M., Johnson, M. D., et al. 2021, ApJ, 912, 35
Palumbo, D. C. M., Wong, G. N., & Prather, B. S. 2020, ApJ, 894, 156
Prather, B., Wong, G., Dhruv, V., et al. 2021, JOSS, 6, 3336
Raymond, A. W., Palumbo, D., Paine, S. N., et al. 2021, ApJS, 253, 5
Ricarte, A., Qiu, R., & Narayan, R. 2021, MNRAS, 505, 523
Walker, M., & Penrose, R. 1970, CMaPh, 18, 265
Wong, G. N., Du, Y., Prather, B. S., & Gammie, C. F. 2021, ApJ, 914, 55
Wong, G. N., Prather, B. S., Dhruv, V., et al. 2022, arXiv:2202.11721